Hierarchy of the macrozone features in Ti-6Al-4V alloy inferred from massive polycrystal plasticity calculations

Xiaolei Chen, L Germain, Stéphane Berbenni

Highlights

- Macrozone features are ranked as a function of their influence on mechanical behavior.
- Massive FFT-based polycrystal plasticity calculations have been reported.
- More than 80 3D polycrystalline aggregates have been generated from EBSD data acquired on Ti64 alloy.
- Intra-granular stress hotspots and slip activity are affected by the macrozone features

Hierarchy of the macrozone features in Ti-6Al-4V alloy inferred from massive polycrystal plasticity calculations

Xiaolei Chen[a,b], Lionel Germain[a,b], Stéphane Berbenni[a,b,*]

[a] *Université de Lorraine, CNRS, Arts et Métiers ParisTech, LEM3, F-57000 Metz, France*
[b] *Laboratory of Excellence on Design of Alloy Metals for low-mAss Structures (LabEx DAMAS), Université de Lorraine, Metz, France*

Abstract

Titanium alloys exhibit complex microstructures containing heterogeneities at different length scales. Microtextured regions (MTRs), usually called "macrozones", exhibit grains having the same or nearly the same crystallographic orientation. They are known to have a detrimental influence on the alloy performance under cyclic loadings and dwell fatigue. Recent numerical studies based on crystal plasticity evidenced an effect of the degree of macrozones on the yield strength and stress distributions in polycrystalline aggregates. In the present study, a fast Fourier transform-based crystal plasticity elasto-viscoplastic (CP-EVPFFT) code using MPI (Message Passing Interface) and the FFTW library, is used to perform massive calculations for the study of the mechanical response in the microplastic stage of large 3D polycrystalline aggregates containing macrozones. These macrozones are synthetically generated with three different features: crystallographic texture with different orientation and intensity, volume fraction, and morphology. The 3D microstructure is obtained from EBSD data measured on a Ti64 hot rolled and annealed plate. Using two metrics, namely the equivalent Von Mises stress and the normal stress to basal plane, which is important for fatigue damage, intra-granular stress hotspots are found to be affected by the presence of the different macrozone features. A slip analysis is reported for a macrozone with a lamina shape. The CP-EVPFFT model predicts an early activity at low strain for 1^{st} order $\langle c + a \rangle$ pyramidal slip when the macrozone exibit a strong $\langle 0002 \rangle$ texture component. The discussion concludes on a hierarchy of these macrozone features for mechanical performance of the Ti64 alloy.

Keywords:

*Corresponding author:
Email address: stephane.berbenni@univ-lorraine.fr (Stéphane Berbenni)

Micromechanics, Titanium alloys, Crystal Plasticity, Macrozones, Simulations

1. Introduction

The presence of macrozones or microtextured regions (MTRs) in titanium alloys is still a concern for components integrity [1]. Macrozones are clusters of grains having close crystallographic orientations or at least close $\langle c \rangle$-axes, which are reported to reduce fatigue life by up to two order of magnitude when the stress is dwelled at peak-stress [2]. Recently, macrozones have been pointed out in two publicly released engine failure investigations reports for Ti-6Al-4V (Ti64) fan blades. In the first one, the presence of macrozones led to a fatal crack formation [3], and in the second one, they guided the fatal crack propagation path [4].

Historically, dwell fatigue debit was first reported in 1972 [5, 6], but macrozones only ten years later. First characterized by X-rays diffraction in 1985 by McDarmaid et al. [7], they were then called "aligned and contiguous α grains". Later, macrozones were rediscovered on optical micrographs in bimodal microstructures by Kansal et al. [8]. This was possible because globularization is influenced by the crystal orientation. With the automatization of EBSD, macrozones identification was done more systematically: first by Woodfield et al. [9], referring to "large primary α colonies" and later to "microtexture" by Bailey et al. [10]. Back then, the term "microtexture" was ambiguous, because it was also used to designate the combined information of microstructure and crystal orientation [11, 12] even in the context of dwell fatigue [13]. Nowadays, "macrozones" [14] and "microtextured regions" [15] abbreviated "MTRs" [16] are commonly used to designate those clusters of grains with close orientations.

The macrozones are the result of an ineffective globularization which failed to randomize the orientations within initially large Widmanstätten colonies inherited from the prior β grains [17, 18]. Randomizing the orientations by producing a bimodal microstructure has only a limited impact. Indeed, the secondary α orientation may still reinforce the local texture when adjacent β and primary α grains are related by the Burgers orientation relationship [19]. One way to decrease macrozones intensity is through an adapted forging route [20] including a very high total strain [21] and isothermal holding to trigger globularization [22]. However, this is easier to achieve in bars or plates than in billets or large forged components. Therefore, in the absence of aeronautical specifications to address macrozones in manufactured products, and despite the considerable efforts put into research to eradicate those, the industry must still live with them [23].

A lot of progress has been made to understand the link between the presence of macrozones and dwell fatigue debit. Early investigations suspected the Stroh mechanism to lead to cleavage facets formation [24]. In this mechanism, adjacent hard and soft grains, called the "rogue grain combination", induce facets formation through load shedding [25]. However, the complexity increases, as one scales the "rogue combination" to a hard-soft macrozones combination [26]. In this case, it is useful to define what is a macrozone? Macrozones can be identified with $\langle c \rangle$-axis orientation only [27] or complete crystal orientation [28]. The angular threshold used varies between 10° and 15° [29], and the size evaluation can be performed by auto-correlation functions [27] or by neighbor-to-neighbor clustering [28].

Several characteristics of the macrozone can influence the mechanical properties of titanium alloys. Liu and Dunne [30] reported that a high aspect ratio ($\gtrapprox 4$) makes macrozones particularly damaging when their long-axis is nearly parallel to the loading direction. The 3D shape of the grains is harder to assess. Experimentally, it was studied by James et al. [31] from 2D measurements, and assuming a prolate shape, although oblate macrozones can also be found in cross rolled plates for example. The orientation of the grains also matters, the worst case being when their $\langle c \rangle$-axis is within about 15° to the principal stress direction [30], whereas soft macrozones seem to act as barrier against crack propagation [32]. Additionally, dislocation content is higher in macrozones [33], as a result of the ineffective globularisation, which influences the mechanical behavior.

Dwell fatigue is well suited to be investigated by crystal plasticity. Indeed, the "rogue combination" is detrimental for dwell fatigue because of both elastic and plastic anisotropies in α-Ti. Indeed, the elastic stiffness along the $\langle c \rangle$-axis, i.e. perpendicular to the (0002)-basal plane, is higher than the one parallel to this plane, and, slip directions for active slip systems, mainly basal and prismatic, lie in the basal plane. Therefore, hard oriented grains have their $\langle c \rangle$-axis parallel to the loading direction. When hard and soft grains are adjacent, the "load shedding" or stress redistribution [5] eventually leads to fatigue crack nucleation near grain boundaries. Then, crystal elastic and/or viscoplastic finite element (CP-FEM) and fast Fourier transform (CP-FFT) micromechanical models are very good candidates to investigate the three-dimensional strain/stress states in polycrystalline aggregates containing macrozones [34, 35, 36, 30, 37, 38]. The advantage of CP-FFT is to include a fast and efficient solver, which directly uses voxelized data (no meshing procedure).

In order to study the respective roles of the different macrozone features in large polycrystalline aggregates like global texture, morphology and volume fraction during the elasto-viscoplastic transition, an elasto-viscoplastic full field model with a FFT solver (CP-EVPFFT) is used. Using experimental EBSD data, different repre-

sentative volume elements with macrozones are generated and fully studied to detect intra-granular stress hotspots in the microstructure. In comparison with Naït-Ali et al. [37], who used a CP-EVPFFT model to investigate macrozone morphology effects, larger macrozone volume fractions and more various morphologies are considered in the present contribution to discuss the hierarchy of the macrozone features in Ti64. Furthermore, we specifically developed a parallelized MPI-based implementation to perform massive voxelixed polycrystalline microstructures with such macrozones.

The paper is organized as follows: In section 2, the material and the main features of the microstructure are presented. The EBSD data are reported and the global crystallographic orientation distribution is discussed. In section 3, the numerical method is introduced. The crystal plasticity (CP)- ElastoViscoPlastic (EVP) fast Fourier transform based (FFT) is applied in the context of small strains, and a parallelized code implementing the CP-EVPFFT formulation was developed using both MPI and FFTW3 libraries. The single crystalline elastoviscoplastic constitutive behavior is also introduced in this section. In section 4, the method to generate different synthetic polycrystalline microstructures from EBSD data with different macrozone features is presented. These periodic Representative Volume Elements (RVEs) are used as inputs of the CP-EVPFFT simulations. In section 5, the numerical results are reported and discussed regarding both macroscopic and microscopic stress responses. In particular, we focus on the analyses of the distributions of Von Mises stress and normal stress to basal plane (i.e parallel to the $\langle c \rangle$-axis). The correlations between these stresses and macrozone features (crystallographic texture and intensities, volume fractions in the RVE and macrozone morphologies), as well as with slip activity, are reported and discussed.

2. Material and microstructure

A specimen was cut out from a hot rolled and annealed plate AIMS 03-18-001 Ti64 for microstructure and texture analysis. The microstructure was composed of equiaxed α grains with a maximum size of 30 µm and about 3% β grains with a maximum size of 5 µm located at the triple points. The microstructure, texture and mechanical properties of this material were already reported [39], but are recalled here for convenience. The microtexture was characterized in a Scanning Electron Microscope (SEM) using Electron BackScattered Diffraction (EBSD). A 2300×560 µm^2 EBSD map was acquired in the ND-RD plane with a step size of 0.8 µm, as shown in Figure 1(a). The map is plotted with the Inverse Pole Figure (IPF) color code with respect to the rolling direction (RD). It presents alternate red and

blue bands corresponding to two classical texture components: $\langle 0002 \rangle$ //RD and $\langle 0002 \rangle$ //TD [40].

From the EBSD maps, four orientation datasets were obtained. The whole orientations were used to produce the texture of the matrix in which the macrozones are embedded (called "non-macrozone" set in the sequel). Then, three clusters of grains were manually selected. The first one is a large cluster of red grains corresponding mainly to the ($\langle 0002 \rangle$ //RD) orientation with a maximum $\langle 0002 \rangle$ mrd. (multiple of random distribution) of 4.7. The second one is a large blue cluster corresponding to the ($\langle 0002 \rangle$ //TD) orientation with a maximum $\langle 0002 \rangle$ mrd. of 30. Since the texture intensities of these two clusters were different, another set was created by keeping in the ($\langle 0002 \rangle$ //RD) only the grains with their $\langle c \rangle$-axis at 15 degrees from RD. These three sets of orientations are named "x", "z-intense" and "x-intense", respectively.

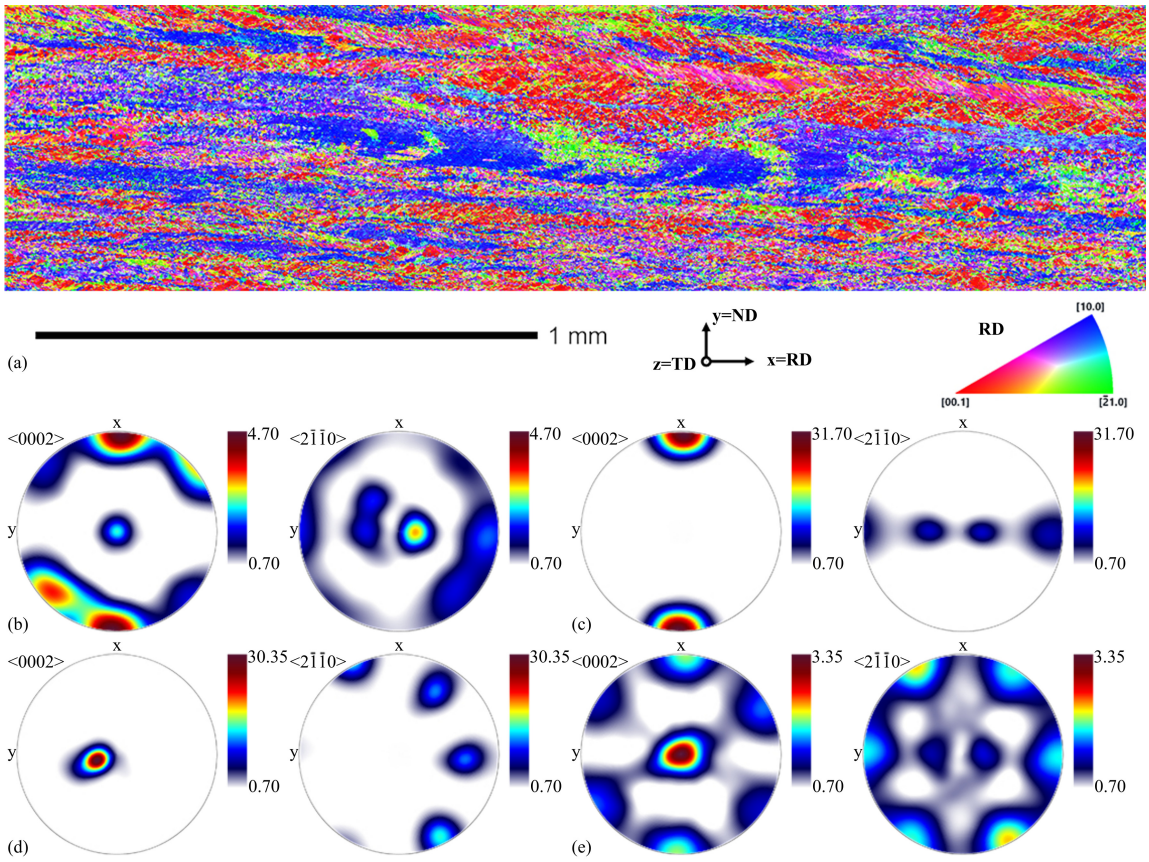

Figure 1: (a) EBSD map of Ti64 plate with bimodal microstructure. Pole figure of the orientation density function (ODF) for the considered textures of (b) x-100%, (c) x-intense-100%, (d) z-intense-100% and (e) texture of the matrix (texture Macrozone-0%). Pole figures were created with the ATEX software [41].

3. Micromechanical model

3.1. CP-EVPFFT model

A Crystal Plasticity ElastoViscoplastic Fast Fourier Transform formulation (CP-EVPFFT) is adopted in a small deformation setting. This formulation was earlier developed by Lebensohn et al. [42], and it is here adapted for parallel computing to study the effect of macrozones for large polycrystalline aggregates in the transcient elasto-viscoplastic regimes under monotonic tensile loadings. In the CP-EVPFFT formulation, an iterative numerical scheme is used to treat the Lippmann-Schwinger equation, which is solved from the Green operator in Fourier space [43, 44, 45, 46, 47].

Besides, the robust Augmented Lagrangian (AL) method is used with the Uzawa descent algorithm [48]. The non linear viscoplastic behavior is handled with a Newton-Raphson's type procedure inside each interaction step, see [42] for more details. In contrast with more classic CP-EVPFFT formulations for studying macrozones using the basic scheme [43], e.g. [37], which are based on a strain-controlled criterion, this condition adopted for the AL method implies the fulfillment of both stress equilibrium and strain compatibility up to a sufficient accuracy. Let us note that the CP-EVPFFT method was recently extended to finite strains with the AL method by Zecevic et al. [49]. However, here only the small strain CP-EVPFFT is used, since the microplastic regime is studied, i.e. the elastoviscoplastic transition at small strains. Regarding the loading condition, a uniaxial tensile test in the x-direction is performed with an applied strain up to 1.5% and a strain rate of $\dot{E}_{11} = 10^{-4}s^{-1}$.

A new Fortran 2003 home made parallelized code of the CP-EVPFFT formulation was specifically developed in LEM3 to study the effects of spatial resolution on the local mechanical fields and on the overall stresss/strain response in the presence of macrozones. The interest of the parallelization is not only for accelerating computation, but also for memory optimization for massive calculations. Here, the code parallelization was achieved with the Message Passing Interface (MPI) and using the efficient FFTW3 library (parallel version) [50], calling the subroutine: `fftwf_mpi_execute_dft`, instead of the original one based on the Numerical Recipes: `fourn` [42]. Here for parallelization, a slab decomposition along the z-direction was applied. The EXPLOR Super Computer Center of the University of Lorraine was used with up to 512 cores. It should be noted that another parallelized code of the CP-EVPFFT formulation was developed by Tari et al. [51] (MASSIF code), and was recently applied to study the elastoplastic transition of a metastable alloy β-Ti (Timetal-18) [52]. Meanwhile, a version of the MASSIF code based on GPU systems has also been developed [53].

3.2. Single crystal's elastoviscoplastic behavior

The studied Ti alloy essentially contains the α phase. Due to their very low volume fraction (see section 2), the β grains are neglected in the present model. The α phase presents a transversely isotropic elastic behavior in the crystal basis related to the $\langle c \rangle$-axis direction. The five independent elastic moduli of the material expressed with the Voigt convention in the crystal basis are reported in Table 1.

C_{11} (GPa)	C_{12} (GPa)	C_{13} (GPa)	C_{33} (GPa)	C_{44} (GPa)
162.4	92	69	180.7	46.7

Table 1: Elastic moduli of single crystal used in the present study [37].

Regarding crystal plasticity, only slip mechanisms were considered for the CP-EVPFFT calculations and 18 slip systems of α-Ti were considered, including three basal slip systems: $(0002)\left\langle 11\bar{2}0\right\rangle$, three prismatic slip systems: $\left\{10\bar{1}0\right\}\left\langle \bar{1}2\bar{1}0\right\rangle$ and twelve 1st order $\langle \mathrm{c}+\mathrm{a}\rangle$ pyramidal slip systems: $\left\{10\bar{1}1\right\}\left\langle \bar{2}113\right\rangle$ [54]. The plastic strain rate tensor $\dot{\boldsymbol{\varepsilon}}^{\mathrm{p}}$ was calculated using a power law as slip rate formula [55]:

$$\dot{\boldsymbol{\varepsilon}}^{\mathrm{p}} = \Sigma_{\mathrm{s}} \boldsymbol{m}^{\mathrm{s}} \dot{\gamma}^{\mathrm{s}} = \Sigma_{\mathrm{s}} \boldsymbol{m}^{\mathrm{s}} \dot{\gamma}_0^{\mathrm{s}} \left(\frac{|\tau^{\mathrm{s}}|}{\tau_{\mathrm{c}}^{\mathrm{s}}} \right)^{n^{\mathrm{s}}} \mathrm{sgn}\left(\tau^{\mathrm{s}}\right) \tag{1}$$

where for each slip system s, $\boldsymbol{m}^{\mathrm{s}}$, $\dot{\gamma}^{\mathrm{s}}$, $\dot{\gamma}_0^{\mathrm{s}}$, n^{s}, $\tau^{\mathrm{s}} = \boldsymbol{m}^{\mathrm{s}} : \boldsymbol{\sigma}$, and $\tau_{\mathrm{c}}^{\mathrm{s}}$ are the symmetric Schmid tensor, the slip rate, the reference slip rate, the power law exponent, the resolved shear stress, and the critical resolved shear stress (CRSS), respectively. $\boldsymbol{\sigma}$ is the Cauchy stress tensor. The symmetric Schmid tensor was defined as $\boldsymbol{m}^{\mathrm{s}} = \frac{1}{2}\left(\boldsymbol{b}^{\mathrm{s}} \otimes \boldsymbol{n}^{\mathrm{s}} + \boldsymbol{n}^{\mathrm{s}} \otimes \boldsymbol{b}^{\mathrm{s}}\right)$, where the unit vectors $\boldsymbol{b}^{\mathrm{s}}$ and $\boldsymbol{n}^{\mathrm{s}}$ denote the slip direction and the slip plane normal, respectively. Then, the values of $\tau_{\mathrm{c}}^{\mathrm{s}}$ were considered to be constant (no hardening effect), which are presented in Table 2 for the 18 slip systems (corresponding to the three slip system families). These values were extracted from the work of Naït-Ali et al. [37] based on the experimental identification procedure reported by Hémery et al. [56]. Meanwhile, $\dot{\gamma}_0^{\mathrm{s}}$ and n^{s} were considered to be identical for all 18 slip systems with the value $\dot{\gamma}_0 = 1.0 \times 10^{-7}$ s^{-1} and $n = 50$ [37, 56].

MPa	basal	prismatic	1st order $\langle \mathrm{c}+\mathrm{a}\rangle$ pyramidal
$\tau_{\mathrm{c}}^{\mathrm{s}}$	338.0	352.0	580.0

Table 2: Values of $\tau_{\mathrm{c}}^{\mathrm{s}}$ for the 3 slip system families in Ti–6Al–4V alloy [37].

4. Synthetic polycrystalline microstructures with macrozones

4.1. Grain size-controlled polycrystalline microstructure

The polycrystals were modelled by periodic Voronoi tessellations by using about 5000 Voronoi seeds. The grain size was strictly controlled to be larger than 250 voxels for all the simulations with a total number of voxels of $128^3 = 2097152$ for the CP-EVPFFT calculation, which was realized by keeping the distances between Voronoi central seeds larger than 3.91 voxels. At the same time, the grain size was also controlled to be as small as possible, optimized by random generation, to prevent from large grain effects. To summarize, the grain volume was well controlled to be between 250 and 650 voxels, with a median of 450 voxels, with the histograms presented in Figure 2. It shows that the grain size follows a log-normal distribution with parameters: $\mu = 6.06$ and $\sigma = 0.14$. This corresponds to an average equivalent

diameter of 9.3 pixels which is well beyond the convention of 10 pixel area used to guarantee a reliable grain size determination from EBSD data [57].

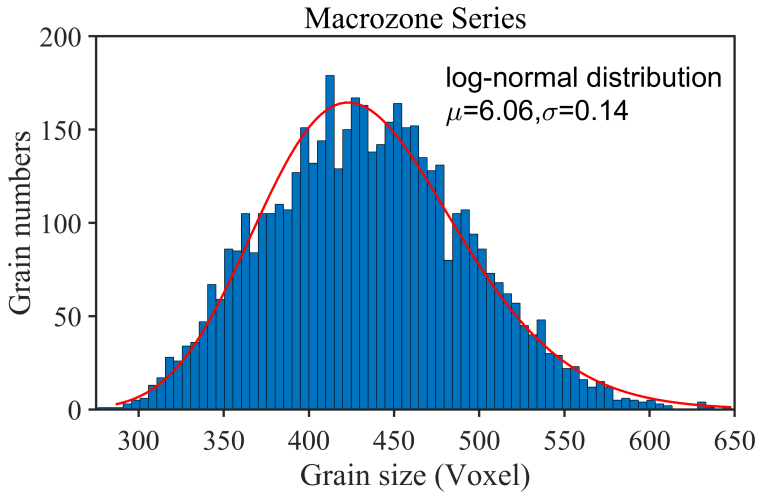

Figure 2: Example of the grain size distribution obtained by controlling the grain size during the Voronoi tessellation. The grain size is given in voxels related to the FFT grid.

4.2. Generation of macrozones with different features

The different macrozone morphologies were modeled in two steps. First, a macrozone was placed in the center of the aggregate. Its shape was set to be either a cylinder with its axis aligned in X or Y, a lamina (planar) with its normal in X or Y or a sphere. Its size was defined as a function of volume fraction occupied. Five volume fractions were selected: 5%, 10%, 20% and 40%. Figure 3 illustrates the different macrozones morphologies for a volume fraction of 40%.

In the second step, if the Voronoi seed falls in the macrozone, its orientation was drawn from the corresponding macrozone texture (Figures 4(a),(b),(c)) or instead from the non-macrozone texture (Figure 4(d)). All aggregates have the same Voronoi polycrystalline configuration, which was randomly constructed under the grain size control conditions (see section 4.1). For each volume fraction and texture, an additional so-called "Random morphology" was generated with the same orientations, but associated with randomly selected Voronoi seeds. All those aggregates are designated by this scheme: "Morphology-Volume Fraction%-Texture". Additionally, 0% and 100% Macrozones microstructures were also generated for comparison purposes except that they do not include any macrozone morphology. Finally, to assess reproducible microstructure generations, variations of the same aggregate were

generated. They are indicated by the aggregate name preceded by "vs.". All the generated aggregates are summarized in Table 3. In total, 84 polycrystalline aggregates were generated for the tensile test simulations with the CP-EVPFFT model.

Macrozone features	Values
Texture	"x" or "x-intense" or "z-intense"
Morphology	Sphere or Cylinder-X (Y) or Lamina-X (Y) or Random
Volume fraction	0% or 5% or 10% or 20% or 40% or 100%

Table 3: Summary of the generated synthetic polycrystalline microstructures with macrozone features and their values.

The crystallographic texture of the Lamina-X-40%-"x-intense" configuration is reported on Figure 4 (e). It should be noted that our simulations are different from those investigated by Naït-Ali et al. [37]. These authors considered the effects of very low macrozone volume fractions up to 7% in order to maintain the global macrotexture. Here, the same objective is achieved because each macrozone morphology can be compared with the corresponding "Random morphology". However, the advantage is here to consider a wider range of macrozone volume fractions.

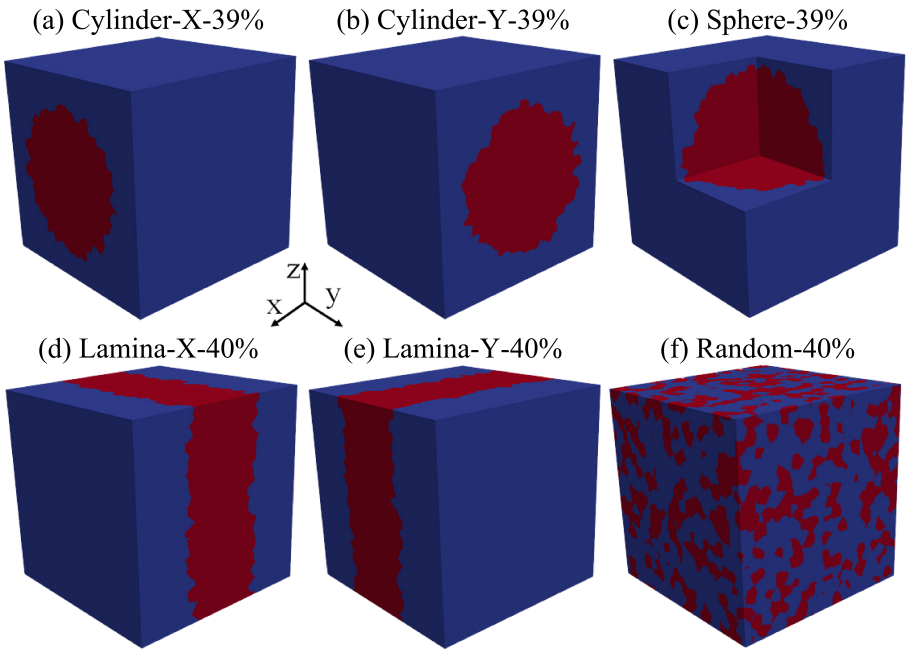

Figure 3: Schematic figures of the considered morphologies of the macrozone with a volume fraction around 40%. The red color indicates the macrozone while the blue is for general grains. The schematic figures for other volume fractions are presented in Appendix A.

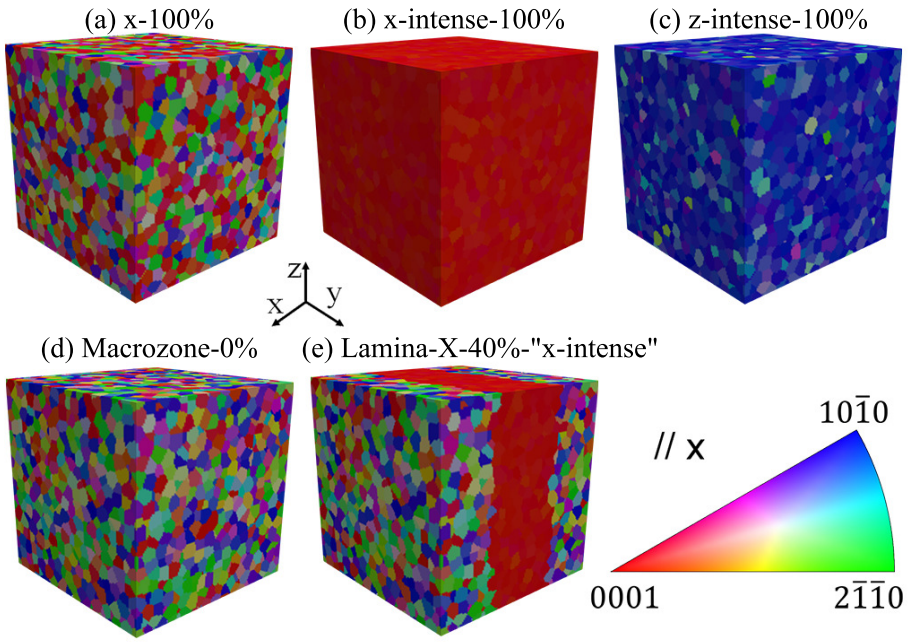

Figure 4: Inverse pole figures (IPF) presenting the crystallographic orientations along the x-direction for the textures of (a) x-100%, (b) x-intense-100%, (c) z-intense-100%, (d) Macrozone-0% and (e) Lamina-X-40%-"x-intense".

5. Results

5.1. Effects of spatial resolution: a convergence study

Massively parallel calculations allowed us to run the model on large RVEs and therefore to study the convergence of mechanical fields for a given polycrystalline microstructure as a function of spatial resolution. The convergence was assessed by performing the same calculation while increasing the number of voxels in the RVE. As an example, the mechanical state of the Lamina-X-40%-"x-intense" configuration reached at the yield point was chosen. First, the influence of spatial resolution on the macroscopic yield stress was assessed. Figure 5(c) shows that the yield stress rapidly converges. Even with 32^3 voxels, the relative error on the yield stress with respect to the case of 512^3 voxels, which is taken as the reference, is only 1.3%. Then, this error is subsequently reduced to 0.43% and 0.18% for 64^3 and 128^3 voxels, respectively. So even at low resolution, the model succeeds in predicting the macroscopic behavior.

However, to study the stress distribution, one also needs to evaluate the local stresses with a good accuracy. Therefore, the Von Mises equivalent stress σ^{eq}, which

contains all stress components, is used as a metric to study numerical convergence on local stresses. It is defined as follows:

$$\sigma^{\text{eq}} = \sqrt{\frac{(\sigma_{11}-\sigma_{22})^2 + (\sigma_{22}-\sigma_{33})^2 + (\sigma_{33}-\sigma_{11})^2 + 6\,(\sigma_{12}^2+\sigma_{23}^2+\sigma_{31}^2)}{2}} \tag{2}$$

The numerical results of this convergence study are reported in Figure 5(a). Here, the Paraview software [58] is used for visualization using the filter option `Cell Data`. It is seen that the edges and shapes of the grain boundaries become clearer and sharper as the number of voxels in the RVE increases. From 128^3 voxels, it is observed that the grain boundary shapes are well defined. Meanwhile, the hotspots of σ^{eq} are extracted and presented in Figure 5(b). These stress hotspots are defined as the voxels having the top 1% highest values of the corresponding stress distribution. It is observed that the hotspots of σ^{eq} are mainly concentrated in the macrozone (see the voxels in red color in Figure 5(b)). With low resolutions (for example 32^3 or 64^3 voxels), it seems that there is not enough statistical representation of the hotspots of σ^{eq}. Then, at least 128^3 voxels are needed to well represent the spatial distribution of stress hotspots in the RVE. It is also clearly observed that outside the macrozone, the stress hotspots are more present close to the interface. To study the local stresses quantitatively, the evaluation of the σ^{eq} profiles along the central line located at the center of yz-plane and along the x-direction for the same microstructure with different voxel numbers are reported on Figure 6(a). It is seen that σ^{eq} exhibits sharp variations at normalized distances of about 0.3 and 0.65 corresponding to the locations of interfaces between the macrozone and the non-macrozone in the x-direction. This result demonstrates that the largest stress incompatibilities are present at the interfaces between the macrozone and non-macrozone regions. A stabilization of the spatial stress profiles is observed from 128^3 voxels. The frequency distributions of σ^{eq} over the RVE are presented in Figure 6(b) for different voxelizations. This shows that at least 128^3 voxels are required in the RVE to well represent the statistics of intra-granular stress, while a RVE of 64^3 voxels still report some slight differences with the reference case. Based on all these previous analyses, we conclude that a RVE with 128^3 voxels is preferred to perform all the following numerical simulations in a reasonable CPU time.

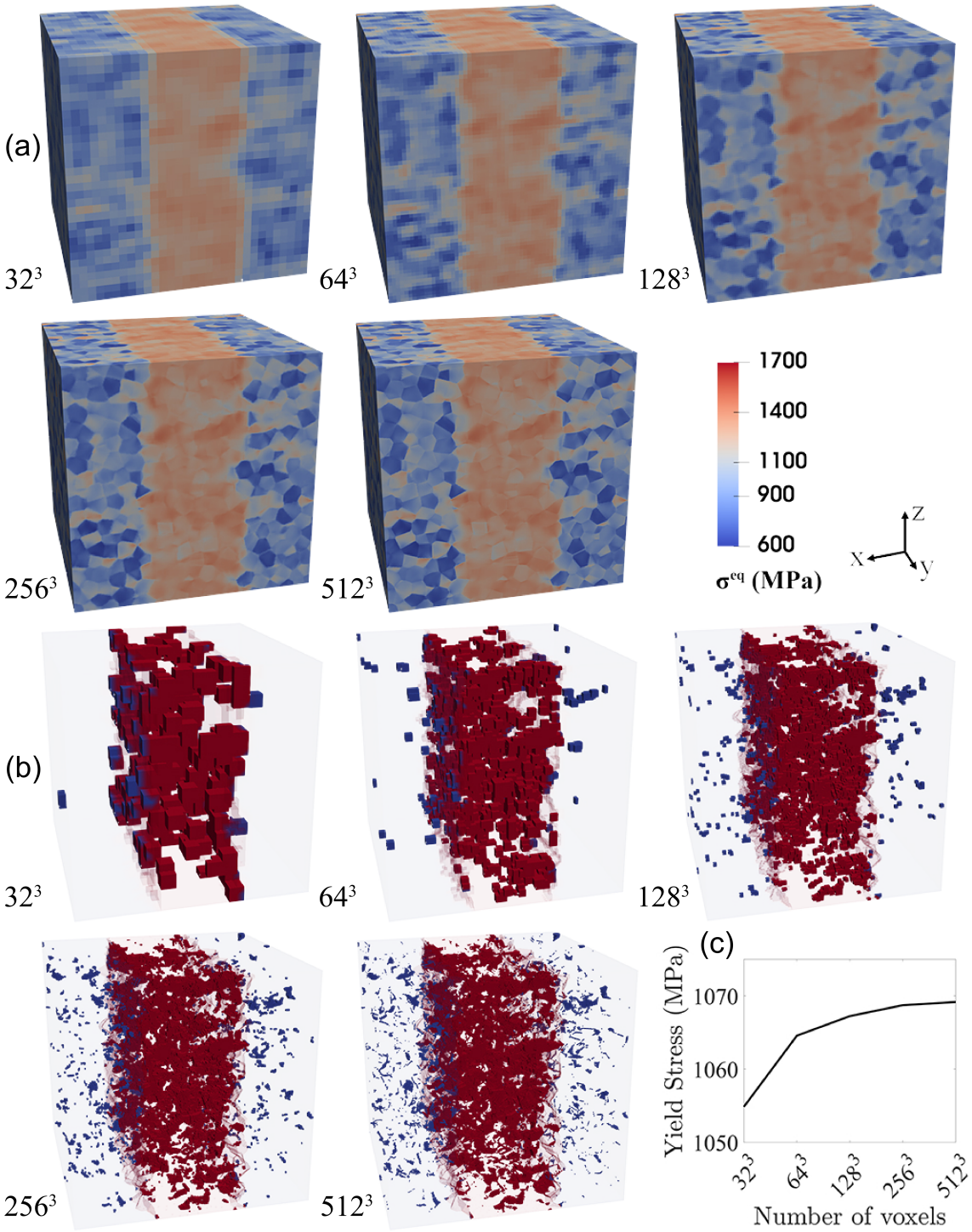

Figure 5: Spatial resolution and convergence assessment at the yield point of the Lamina-X-40%-"x-intense" configuration: (a) spatial distribution of σ^{eq}, (b) location of the σ^{eq} hotspots and (c) overall yield stress as a function of voxel numbers.

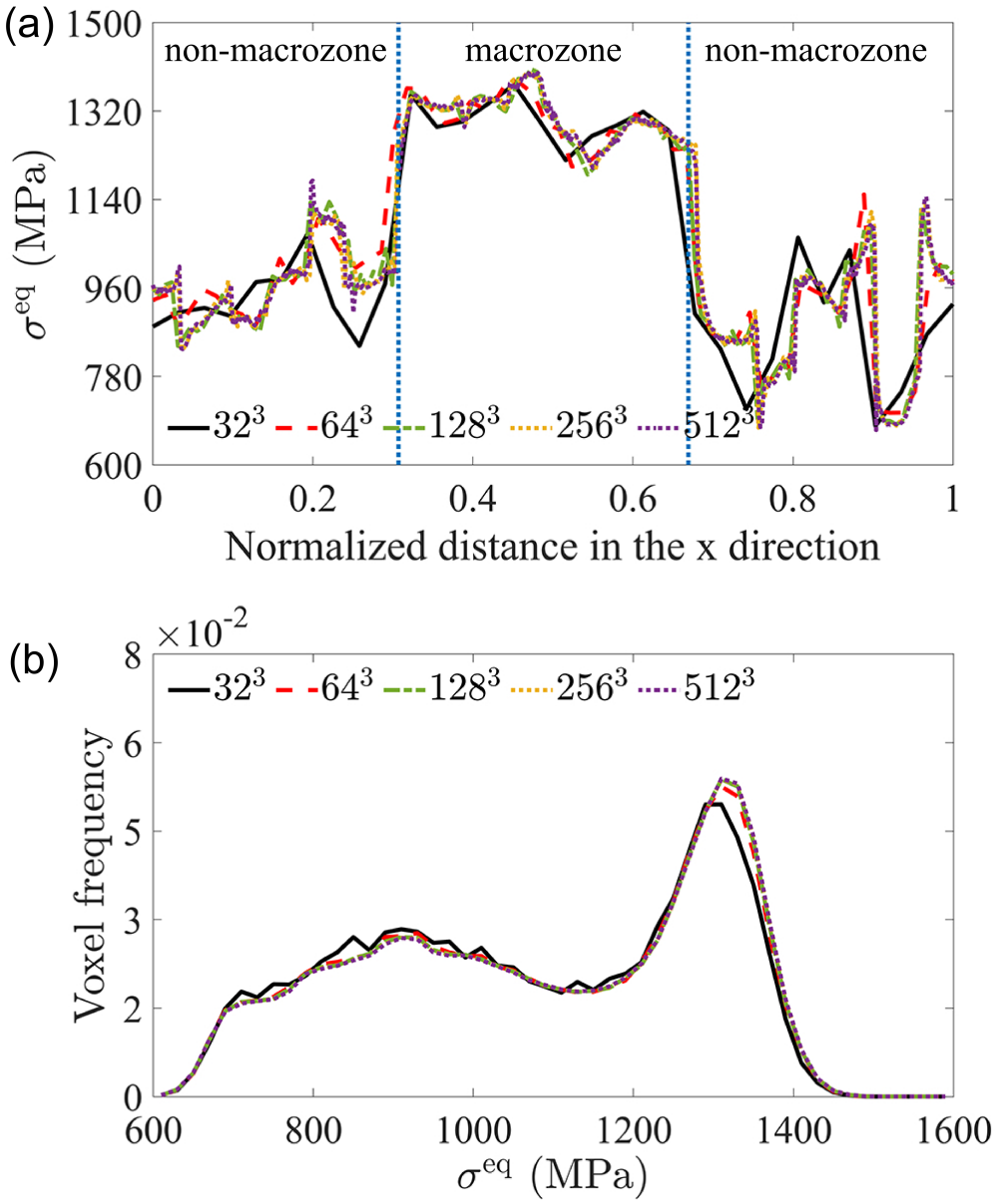

Figure 6: Convergence assessment at the yield point of the Lamina-X-40%-"x-intense" configuration: (a) σ^{eq} estimates along the central line located at the center of yz-plane and in the x-direction, where the blue dotted lines indicate the boundary positions between the macrozone and the non-macrozone, and (b) frequency distributions of σ^{eq}.

5.2. Materials parameters

The material parameters used in the present CP-EVPFFT model for Ti64 are the same as those reported by Naït-Ali et al. [37]. In order to show the ability of these materials parameters to reproduce the alloy's mechanical behavior, the stress-strain curve of the Macrozone-0% configuration was simulated and compared to the experimental tensile curve obtained for the specimen described in section 2. This choice stems from the crystallographic texture of the Macrozone-0% configuration, which is similar to the experimental one. The macroscopic tensile curves are shown in Figure 7(a), and present a good agreement. It is noteworthy that the sharp transition between elastic and plastic regimes observed on the experimental stress/strain curve was also reported on similar alloys [59, 60]. The experimental curve shows that the stress does not increase much in the course of plastic deformation, which demonstrates that the studied material does not have significant hardening after a high yield point. Therefore, the intra-crystalline strain-hardening effect in the single's crystal model was disregarded, as described in section 3.2.

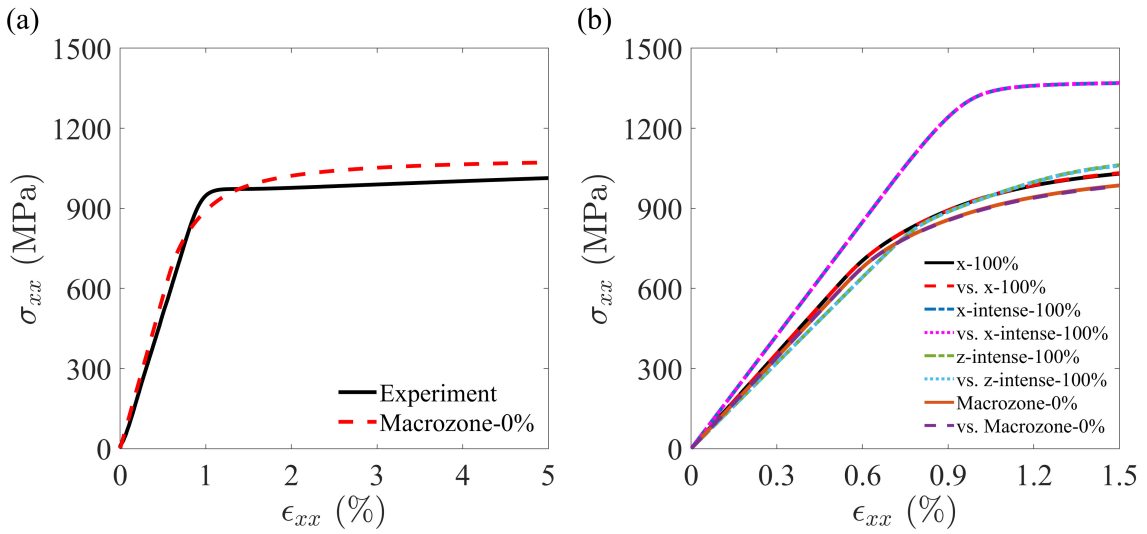

Figure 7: (a) Comparison between the simulated (dotted line) and the experimental (solid line) tensile curves (true stress-true strain curves) (b) True stress-true strain curves for the considered crystallographic textures and their comparison configurations (marked by vs. as defined in section 4.2).

5.3. Influence of macrozone crystallographic texture on the macroscopic tensile stress response

Different random Voronoi configurations generated in section 4 were used to study the effects of the Voronoi configuration on the macroscopic stress-strain curves. Only the extreme cases were considered: Macrozone-0% and Macrozone-100% with different textures. The simulated stress-strain curves are reported on Figure 7(b). Varying the position of the crystal orientations inside the Voronoi tessellation has no influence on the macroscopic behavior, only the macroscopic texture matters. In particular, for the "x-intense" texture, the macrozone leads to a significant increase of the material's yield stress and macroscopic Young's modulus, compared to the general texture (Macrozone-0%). Then, with the "z-intense" texture, the yield stress is a little increased by the macrozone, while the macroscopic Young's modulus is reduced.

5.4. Influence of the macrozone volume fraction and morphology on the macroscopic tensile stress response

Varying macrozone morphologies and textures at constant volume fraction (Figures 8(a-b)) show little influence on the macroscopic behavior, especially with the "x" and "z-intense" textures. An increase of the volume fraction of the macrozone with the "x-intense" texture increases more the macroscopic stress for a given strain. As an example of such effect, the stress-strain curves for the Lamina-X morphology with the "x-intense" texture but different volume fractions are presented in Figure 8(a). Figure 8(b) shows the estimate of the yield stress as a function of the volume fraction of the macrozone for different morphologies and textures. The yield stress always grows up with the macrozone volume fraction for all considered textures. This is in contrast with the work of Naït-Ali et al. [37], who investigated more limited macrozone volume fractions and who reported a softening effect due to macrozones. In particular, it is observed here that the "x-intense" texture significantly increases the yield stress compared to the other textures. The reason is that it is more difficult for basal and prismatic slip to activate for tensile deformation in the x-direction, see section 5.5. Hierarchically, following Figure 8(b), it seems that the macrozone's crystallographic orientation together with its volume fraction exhibit the first order roles on the macroscopic curve, while the effect of morphology appears to be secondary. However, at a fixed volume fraction of macrozone, let say 40% with the "x-intense" texture (see Figure 8(b)), the different morphologies are responsible for an increase of the yield stress with respect to the "Random morphology". Figure 8 (c) and (d) show the effects of morphology on the elastoplastic transition (up to 1.5% of the overall total strain) at fixed "x-intense" texture and volume fractions for 5-6% and 39-40%, respectively. It is observed that for same volume fractions, the morphology

leads to a slight hardening effect compared to the "Random morphology". The most important hardening effect of the morphology is found for Lamina-Y and Cylinder-X morphologies.

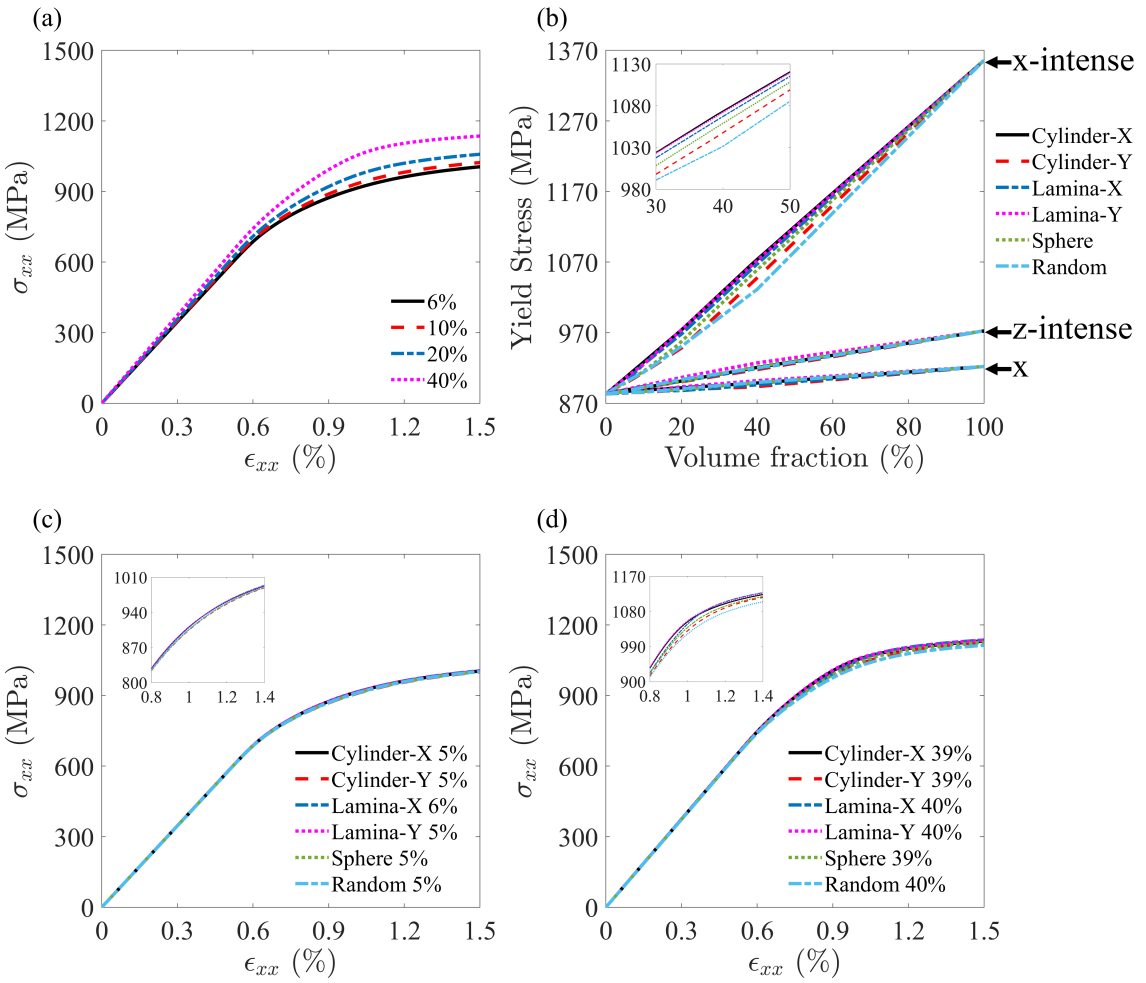

Figure 8: (a) True stress-true strain curves for different volume fractions of the Lamina-X morphology with the "x-intense" texture and (b) Yield stress as a function of the volume fraction of the macrozone with different morphologies for the considered macrozone textures. True stress-true strain curves for different morphologies with (c) 5% and (d) 40% volume fractions of the macrozone with the "x-intense" texture.

5.5. Intra-granular field distributions: Von Mises stress and stress normal to basal plane

The fatigue damage is strongly influenced by the interaction of the shear stress and the normal stress [36, 61, 62]. In the present paper, both the Von Mises stress (σ^{eq}), see Eq. 2, and the normal stress to the basal plane (σ^{n}) are discussed. σ^{n} is defined as:

$$\sigma^{\mathrm{n}} = \sigma_{ij} n_j n_i \tag{3}$$

where $\boldsymbol{n}$ is the unit normal vector of the basal plane.

The spatial distribution of σ^{eq} and σ^{n} is illustrated in Figures 9(a-c) and (d-f), respectively, with the Lamina-X-40% configuration, at the yield point for different textures. Meanwhile, the corresponding evaluations along the central line located at the center of the yz-plane and along the x-direction are presented in Figures 10(a) and (b) for σ^{eq} and σ^{n}, respectively. These two stress metrics exhibit similar distributions following the macrozone location for the three considered textures.

It is seen that the "x-intense" texture leads to much higher values of stresses within the macrozone (compared to the non-macrozone region). The reason lies in the fact that the loading direction (tension in the x-direction) is parallel to the $\langle c \rangle$-axis in the macrozone, enhancing higher values for σ^{n}. From the literature, it was reported in the case of dwell fatigue that crack growth rate in the macrozones is increased when the $\langle c \rangle$-axis is aligned with the loading direction [63]. Therefore, σ^{n} appears to be a good metric in our simulations to account for the macrozone effects on mechanical responses. Stress relief is not allowed in the macrozone due to slip lying in the basal and prismatic planes, which also explains that σ^{eq} exhibit higher values in the macrozone. In the case of the "z-intense" texture, σ^{eq} and σ^{n} have generally lower values in the macrozone. In this case, the loading direction is parallel to the basal plane so that σ^{n} vanishes. Meanwhile, the basal and the prismatic slip systems are prone to activate (see section 5.6), and therefore the Von Mises stress σ^{eq} is relieved in the macrozone. Comparing the results between the "x" and "x-intense" textures, it is found that the texture intensity factor remains crucial for the mechanical properties of Ti64 alloy. In particular, with the "x-intense" texture, the highest concentrations of σ^{eq} and σ^{n} are located in the macrozone.

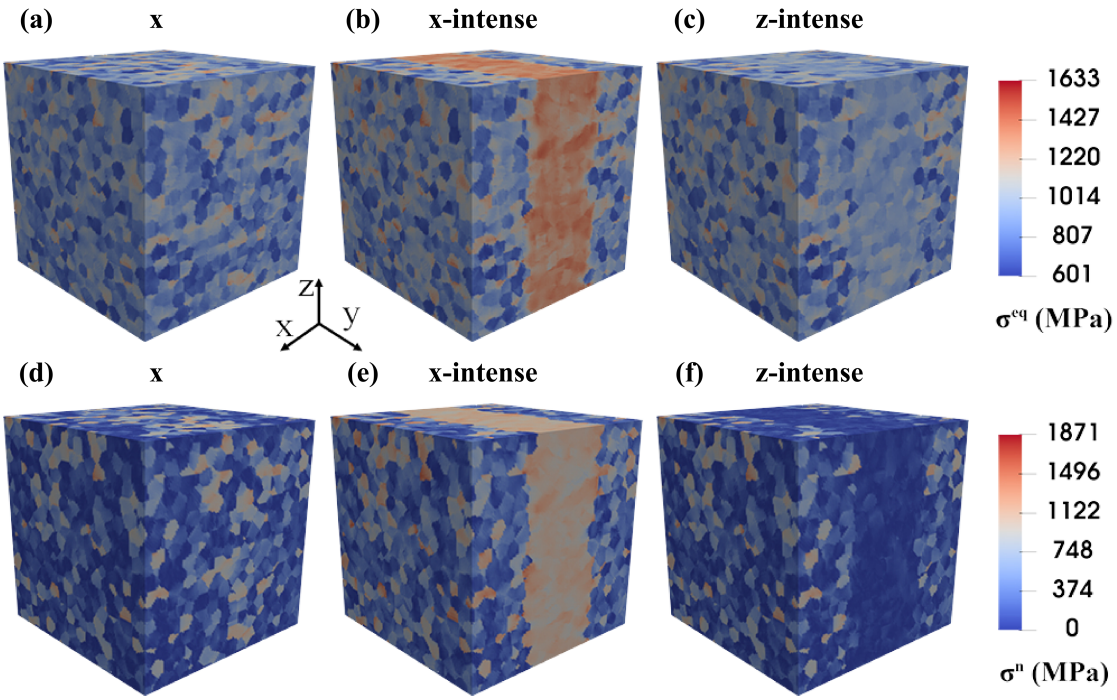

Figure 9: Spatial distribution of (a-c) equivalent Von Mises stress σ^{eq} and (d-f) normal stress to basal plane σ^{n}.

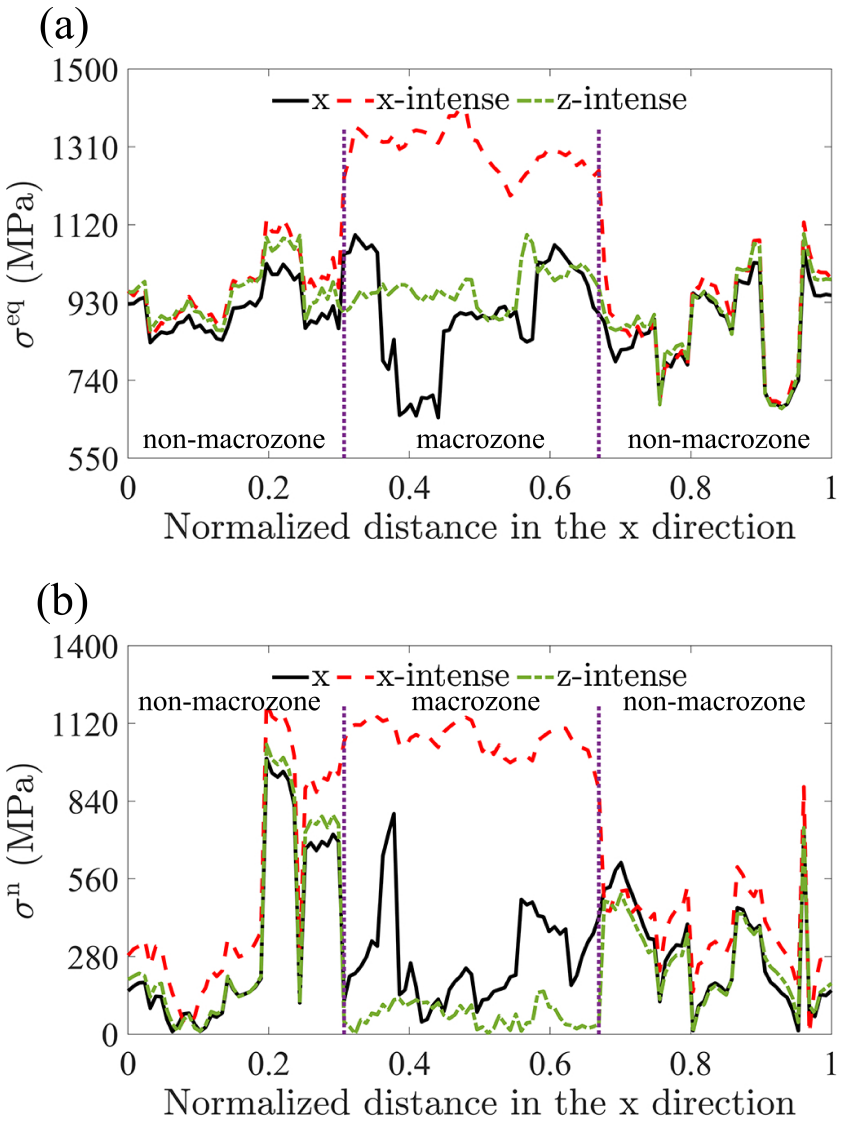

Figure 10: Spatial profiles extracted from Figure 9 along the central line located at the center of yz-plane and along the x-direction for (a) σ^{eq} and for (b) σ^{n} at the macroscopic yield point in Lamina-X-40% configuration with different textures. The purple dotted lines highlights the positions of the boundaries between the macrozone and the non-macrozone regions.

The distribution frequencies of σ^{eq} and σ^{n} fields are presented in Figures 11(a-c) and (d-f), respectively, for different mechanical states with the volume fraction around 40% of different macrozone morphologies with the "x-intense" texture. Only three mechanical states are considered for illustration: the elastic state (at 0.02% of

the overall elastic strain), the plastic yielding state (at 0.2% of the overall plastic strain) and the elastoplastic state (at 1.5% of the overall total strain). Distribution tails at higher stresses present characteristic peak stress values. It is observed that Cylinder-X and Lamina-Y morphologies have similar distribution frequencies for both σ^{eq} and σ^{n} in all three considered states. Their distribution frequency peaks occur at larger stresses than for the other morphologies. Interestingly, in the elastoplastic state, all morphologies lead to similar distribution frequencies for σ^{eq} except for the random case. Indeed, the σ^{eq} frequency distributions for the random case always differ from the other morphologies, see Figures 11(a-c). Their peak stress values are always smaller than those obtained from other morphologies. Then, there is no such significant stress concentration in the absence of macrozones. Therefore, considering the crystallographic texture alone is not sufficient for determining the local distribution of stresses in the Ti64 alloy. These observations demonstrate that the mechanical behavior of Ti alloys is strongly influenced by the presence of the macrozone, and specially by their morphology. In particular, the Cylinder-X and Lamina-Y morphologies generate larger stress concentrations for both σ^{eq} and σ^{n} than other morphologies. These morphologies both have their long axis parallel to the loading direction. Furthermore, it is observed that the scatter of σ^{n} in the distribution frequencies is larger than for σ^{eq}.

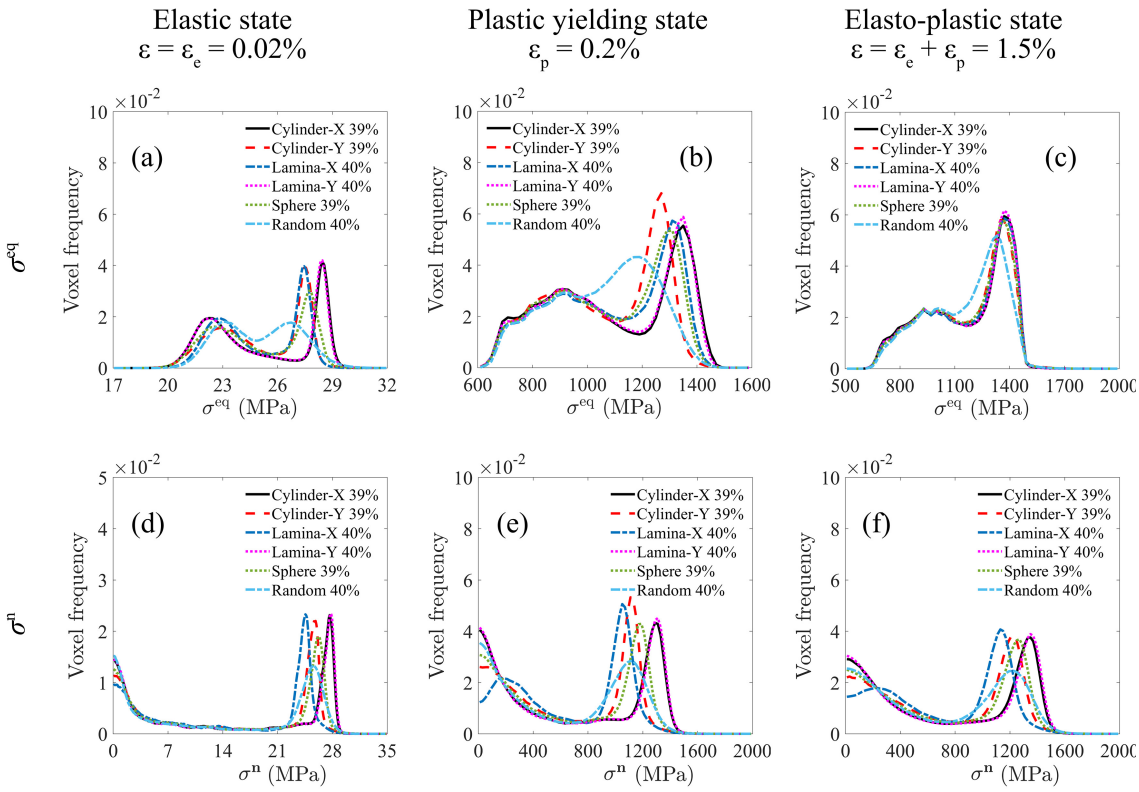

Figure 11: Distribution frequencies of (a-c) σ^{eq} and (d-f) σ^{n} for different mechanical states with a volume fraction around 40% for different macrozone morphologies (including the random case) with the "x-intense" crystallographic texture.

The distribution frequencies of σ^{eq} and σ^{n} are presented in Figures 12(a-f) and (g-l), respectively, for different macrozone morphologies and volume fractions at the yield point with the "x-intense" texture. Different morphologies result in different peak stress values regarding distribution tails (highest stresses). This is related to the stress concentration within the macrozone, as shown in Figures 9(b) and (e) for σ^{eq} and σ^{n}, respectively. More specifically, these peak stress values increase with the volume fraction of the macrozone, except for Cylinder-X and Lamina-Y, where they are almost constant, and already reach their maximum even at low volume fraction. Regarding the random case, there are still peak stress values for σ^{n} with different volume fractions of the macrozone, but there is no evident peaks for σ^{eq} up to a macrozone volume fraction of 40%. In particular, at a macrozone volume fraction of 40%, the value of the peak stress at the distribution tails for both σ^{eq} and σ^{n} with the random case is significantly smaller than those for other morphologies.

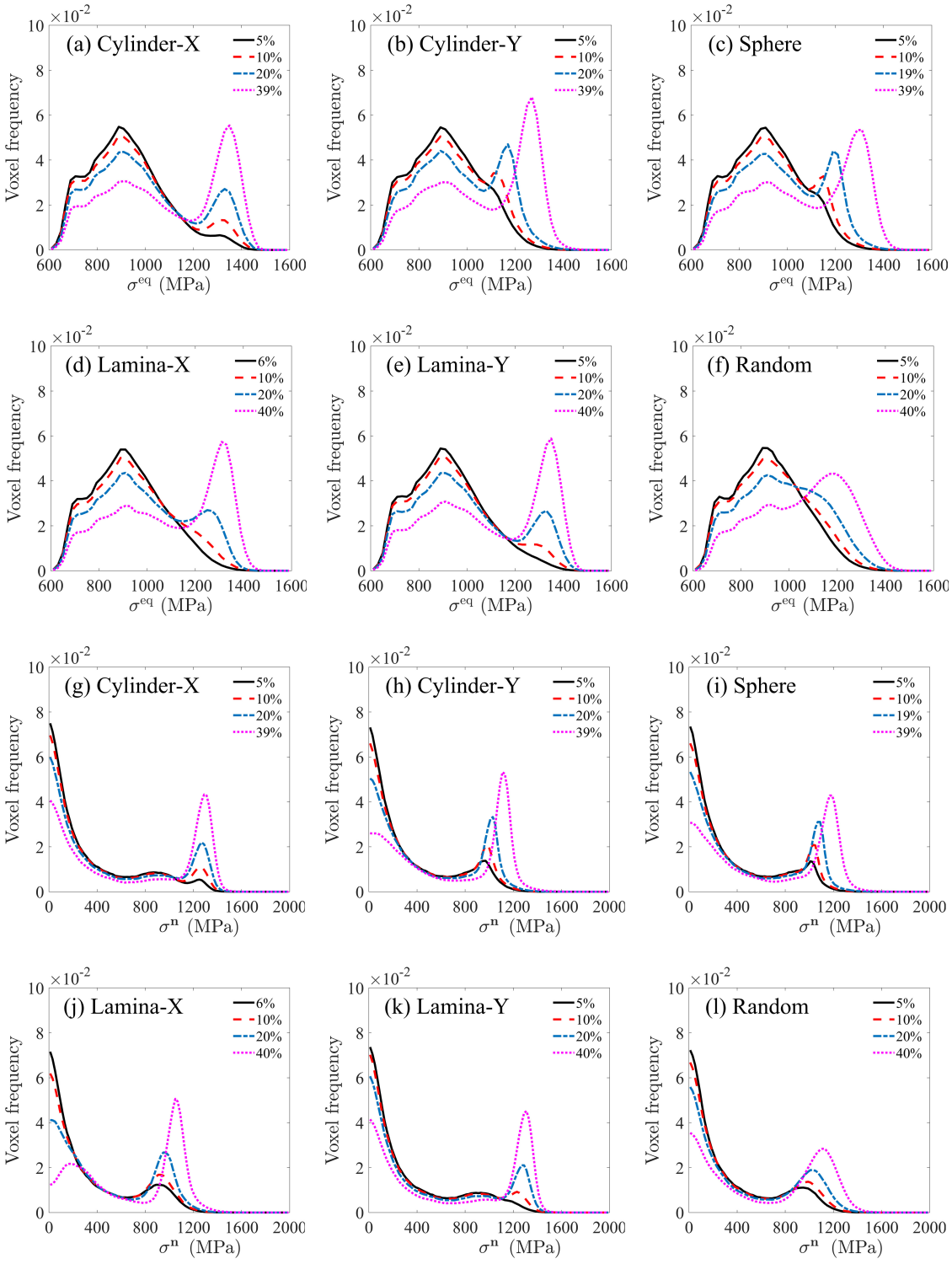

Figure 12: Frequency distributions of (a-f) σ^{eq} and (g-l) σ^{n} at the yield point with the "x-intense" texture as a function of macrozone volume fractions for different morphologies, including the random case.

5.6. Correlation between slip activity and stress hot spots: role of macrozone texture

In order to further analyze the possible correlations between slip activity and stress hotspots as reported in section 5.5, the chosen metric is based on the maximum slip rate $|\dot{\gamma}_{\max}|$, which is a direct output information of the CP-EVPFFT model at each voxel.

The frequency distributions of $|\dot{\gamma}_{\max}|$ for each slip system at voxels with hotspots of σ^{eq} and σ^{n} are reported on Figures 13(a-c) and (d-f), respectively. The distributions are recorded at the yield point for the Lamina-X-40% configuration with different textures. In general, for both σ^{eq} and σ^{n} and for all three considered textures, the values of $|\dot{\gamma}_{\max}|$ with the highest frequency at the peaks are between 1.2×10^{-4} s^{-1} and 2×10^{-4} s^{-1} especially for basal and prismatic slips represented by black and red solid lines. Then, the "x" and "x-intense" textures have relatively similar frequency distributions for both σ^{eq} and σ^{n}, as basal slip appears to be the most active, followed by prismatic slip, while 1$^{\text{st}}$ order $\langle \text{c} + \text{a} \rangle$ pyramidal slip is less activated (blue solid lines). However, Figures 13(b) and (e) demonstrate that 1$^{\text{st}}$ order $\langle \text{c} + \text{a} \rangle$ pyramidal slip is more prone to activate in stress hotspots for the "x-intense" texture, where peaks with highest frequencies are clearly visible at values around 1.0×10^{-4} s^{-1} and 1.2×10^{-4} s^{-1} for σ^{eq} and σ^{n}, respectively. In particular, at the hotspots of σ^{eq} with the "x-intense" texture, all grains are already in a plastic state with a non negligible activation of 1$^{\text{st}}$ order $\langle \text{c} + \text{a} \rangle$ pyramidal slip, while there are always grains remaining in an elastic state for the other cases. In the case of the "z-intense" texture, the differences between basal and prismatic slip activity in stress hotspots are not as large as for the "x" and "x-intense" textures. Meanwhile, for this texture, 1$^{\text{st}}$ order $\langle \text{c} + \text{a} \rangle$ pyramidal slip is clearly less active than other systems in the stress hotspot locations. Based on these results, basal and prismatic slip systems generally contribute to slip activity at the hotspots of both σ^{eq} and σ^{n}. However, it is seen than 1$^{\text{st}}$ order $\langle \text{c} + \text{a} \rangle$ pyramidal slip is more frequently present in the case of the "x-intense" texture at the hotspots of σ^{eq} and σ^{n}, which can be correlated to higher stresses localized in the macrozone, as evidenced in Figures 9(b)(e) and 10. Hence, the macrozone defined with the "x-intense" texture (at fixed morphology and volume fraction in the case of Lamina-X-40%) disturbs slip activity with more probable occurrence of 1$^{\text{st}}$ order $\langle \text{c} + \text{a} \rangle$ pyramidal slip.

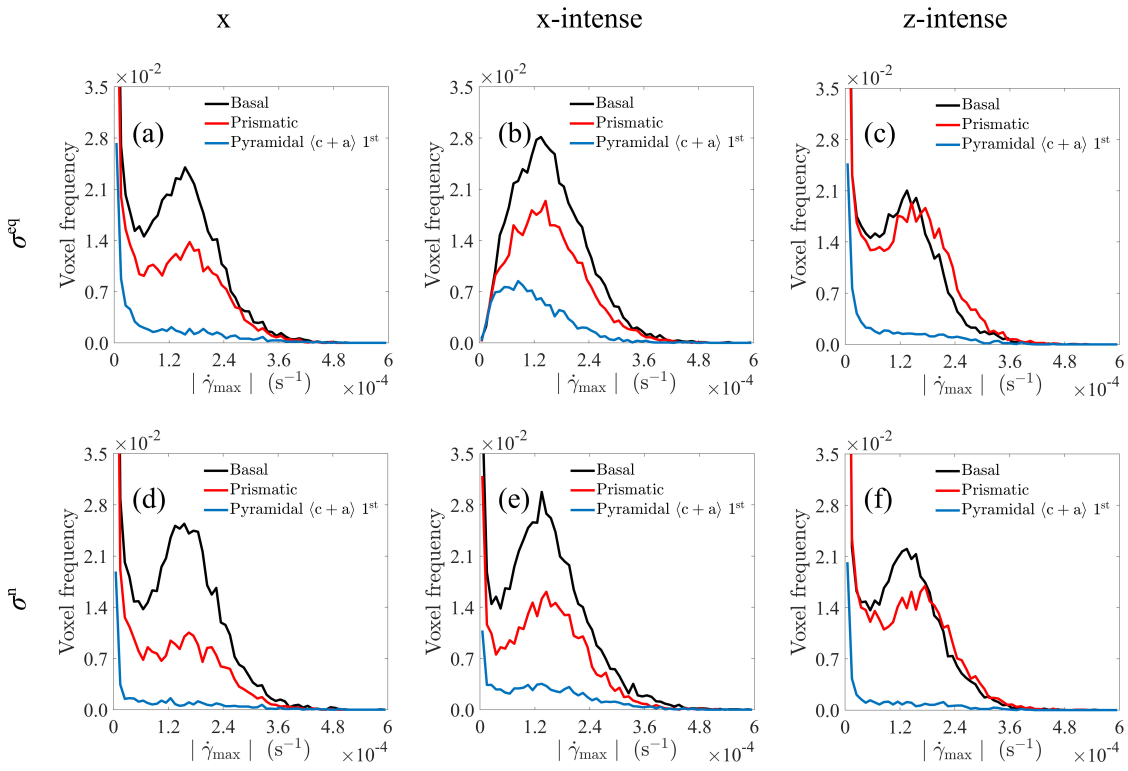

Figure 13: The frequency distributions of $|\dot{\gamma}_{\max}|$ for each type slip system at the hotspots of (a-c) σ^{eq} and (d-f) σ^{n} at the yield point in the Lamina-X-40% configuration with different textures.

To confirm this trend, the relative slip plane family activities calculated in the macrozone and outside the macrozone are now studied. The parameter $\alpha_{\mathbf{sf}}$ defining the overall slip activity is defined as:

$$\alpha_{\mathbf{sf}} = \frac{\sum_{v=1}^{n_v} \sum_{\mathrm{s=p}}^{q} |\dot{\gamma}_v^{\mathrm{s}}|}{\sum_{v=1}^{n_v} \sum_{\mathrm{s}=1}^{n_s} |\dot{\gamma}_v^{\mathrm{s}}|} \tag{4}$$

where n_v is the total number of voxels in a particular domain (i.e. macrozone and non-macrozone), p and q are the first and the last slip system number of the slip family, and $n_s = 18$ is the total number of slip systems.

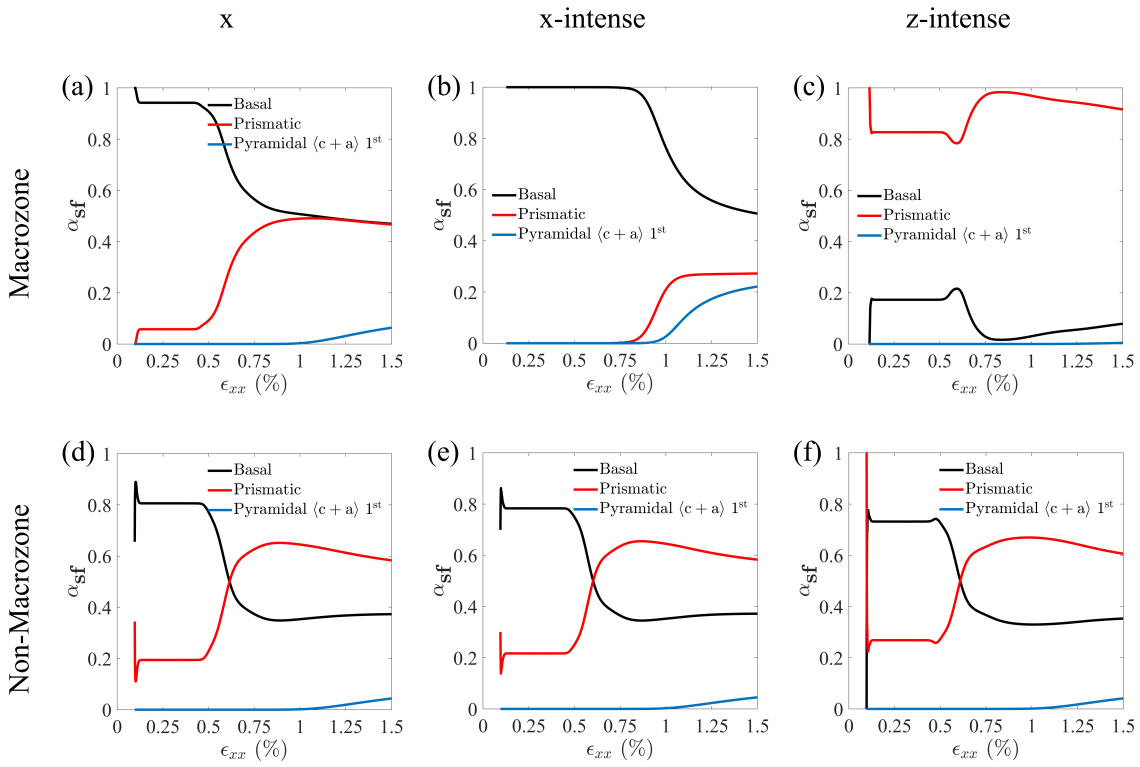

Figure 14: Relative slip plane family activities (dimensionless factor $\alpha_{\mathbf{sf}}$) as a function of the macroscopic strain up to 1.5% in (a-c) the macrozone and (d-f) the non-macrozone in the Lamina-X-40% configuration with different textures.

Figure 14 reports the evolution of $\alpha_{\mathbf{sf}}$ in the course of plastic deformation up to 1.5% tensile strain, for the macrozone and the non-macrozone in the Lamina-X-40% configuration with different textures. It first shows for "x" and "x-intense" textures, that basal slip is active at the onset of plasticity before the macroscopic yield point, then prismatic slip is activated later. For the macrozone with "z-intense" texture (Figures 14(c)), prismatic slip is mainly activated, while basal slip is much less active. Interestingly, while prismatic and basal slips are predominant in the non-macrozone with stabilized slip activities (Figures 14(d-f)), it appears that the scenario is changed in the macrozone with a strong influence of the texture on slip activities (Figures 14(a-c)). This result is consistent with the recent in situ SEM-DIC measurements reported by Echlin et al. [60]. In the case of the "x-intense" texture (Figure 14(b)), it confirms the increase of 1st order $\langle c + a \rangle$ pyramidal slip at low strain (around 1% tensile strain), which is similar to the slip activity observed in $\langle 0002 \rangle$ oriented macrozones by Echlin et al. [60] (see their Figure 13(b) and their

conclusions). Clearly, the relative slip analysis in the macrozone with "x-intense" texture, i.e. $\langle 0002 \rangle$ oriented macrozone (Figure 14(b)), shows that at low strain 1st order $\langle c + a \rangle$ pyramidal slip enters into competition with prismatic and basal slip systems. Since pyramidal slip is less favorable due to higher critical resolved shear stress in the model (see Table 2), this also explains that stress relief is more difficult in this particular macrozone, and prone to earlier crack formation and propagation.

5.7. Hierarchy of macrozones features and their relationship with processing of Ti64 parts

The most important feature of a macrozone lies in its crystallographic orientation and intensity. As reported in previous works [29, 30], the worst configuration is when the $\langle c \rangle$-axis are within a tolerance of 15° to the loading direction. In contrast, when the scatter in the macrozone orientation is high (like in the "x" texture) or when the $\langle c \rangle$-axis is at 90° of the tensile direction (like in the "z-intense"), no significant effect was found.

The two other studied features are volume fraction and morphology. Two morphologies have been reported to be very damageable even at low volume fraction. They have their long axis aligned with the loading direction. For other morphologies, the effects of macrozones were noticeable at higher volume fraction of at least 20%. The only exception to these effects is the Lamina-Y-5%. This one is particular in the sense that it was discontinuous. Indeed, with the chosen Voronoi partition, the 5% volume fraction should have been one grain thick but some holes were present in the Lamina. This probably moderated the effects of the macrozones, revealing thereby the importance in continuity specially in very thin macrozones.

In manufactured titanium parts, macrozones never exhibit cylinder or lamina morphologies. However, oblate and prolate macrozones with a very high aspect ratio are frequently observed. Oblates form as a result of uniaxial compression and prolates would occur more after drawing or cogging. The macrozone morphologies can be revealed by flowlines using macroetching of the parts. For example, the fan blade at the origin of the accident mentioned in the introduction were obtained by cross rolling. Therefore having a high probability to include macrozones with an oblate shape with their short axis perpendicular to the blade thickness. The macroscopic texture of such cross-rolled plate shows a main $\langle 0002 \rangle$ texture component in the normal direction, which should not be a problem for local stresses. However, a small but non negligible fraction of grains have their $\langle c \rangle$-axis pointing radially, which could be more detrimental. This illustration just aimed at showing how flowlines in forged part and local texture analysis could be coupled to infer the risk of having a badly oriented macrozone locally. Therefore, such an approach can be applied to improve

part manufacturing in future.

6. Conclusions and perspectives

The influences of the macrozone features on the mechanical properties of the Ti-6Al-4V alloy were investigated through CP-EVPFFT numerical simulations. In order to perform massive calculations with a large number of grains to refine mechanical field statistics in reasonable CPU times, a homemade parallelized version of the CP-EVPFFT code was developed using both MPI and FFTW3 libraries. Meanwhile, the spatial convergence was analyzed based on the numerical estimate of σ^{eq} for different spatial discretizations from 32^3 to 512^3 voxels. The mechanical influence of the presence of macrozone on the alloy's tensile response in the x-direction was investigated using two metrics based on the equivalent Von Mises stress (σ^{eq}) and the normal stress to the basal plane (σ^{n}). Three macrozone features were analyzed: its crystallographic texture ("x", "x-intense" and "z-intense"), its volume fraction (around 5%, 10%, 20% and 40%) and its morphology (Cylinder-X, Cylinder-Y, Lamina-X, Lamina-Y, Sphere). The following conclusions hold:

- It is shown that, regarding both macroscopic tensile responses and intra-granular stress fields, a RVE with 128^3 voxels is relevant to perform all numerical simulations with different macrozone morphologies in a reasonable CPU time.
- The tensile yield stress increases with the presence of the macrozone for all three considered textures, and, is quasi linearly related to the volume fraction of the macrozone.
- Among the three considered textures, the "x-intense" texture exhibits the largest effect on the macroscopic yield stress, and on stress hot spots for both metrics σ^{eq} and σ^{n}.
- For a given texture at fixed macrozone volume fraction, the macrozone morphology modifies the yield stress with respect to the "Random morphology".
- For the "x-intense" texture, there is a slight increase of the yield stress when a morphology is considered. This increase is more important for Cylinder-X and Lamina-Y morphologies with a volume fraction of 40%.
- Meanwhile, the Cylinder-X and Lamina-Y morphologies are responsible for larger stress values, i.e. stress hotspots, in comparison with other morphologies and a random spatial dispersion of macrozones. These specific morphologies

have been reported to be very damageable even at low volume fraction, which have their long axis aligned with the loading direction.

- At fixed macrozone volume fraction, the influence of the considered macrozone features can be ranked as follows: crystallographic texture intensity > > morphology. At fixed crystallographic texture with fixed volume fraction of macrozone, macrozone shapes with their long axis aligned with the tensile direction may be detrimental for Ti64 alloy performance.

- In the macrozone with the "x-intense" texture, 1st order $\langle c + a \rangle$ pyramidal slip occurs at low strain (around 1% tensile strain), which is consistent with the experimental results reported by Echlin et al. [60].

The present CP-EVPFFT simulations with large polycrystalline aggregates easily allow to analyze intragranular mechanical fields and slip activities, especially around material defects as macrozone, or at the interface between the macrozone and the non-macrozone. However, the experimentally macroscopic stress-strain curves cannot provide intra-granular details to validate the crystal plasticity model at this level. Therefore, as a future work, Digital Image Correlation (DIC) to obtain the strain field, and slip analyses will be performed to be compared with the outcomes of the model. In addition, it is also expected to apply the recent augmented non local crystal plasticity-based MFDM-EVPFFT model [64] in a homemade parallelized version to study the combined effects of grain and macrozone sizes on the macroscopic responses and on stress hotspots for Ti alloys.

Funding

The authors are grateful to the French State (ANR) through the program "Investment in the future" (LabEx "DAMAS" referenced as ANR-11-LABX-0008-01) for financial support.

Acknowledgments

The authors acknowledge Ricardo Lebensohn of the Los Alamos National Laboratory (USA) for providing us the original CP-EVPFFT code, from which we developed in the present work a parallelized version using MPI, and Eric Fleury (LEM3, University of Lorraine, France) for providing us EBSD and tensile test data for the Ti-64 rolled plate. High Performance Computing resources have been provided by the EXPLOR center hosted by the University of Lorraine (Project 2021M4XXX2438).

References

[1] A. Pilchak, M. Gram, Cold dwell fatigue of titanium alloys, JOM 74 (10) (2022) 3691–3692. doi:10.1007/s11837-022-05463-1.

[2] W. J. Evans, The influence of microstructure on dwell sensitive fatigue in a near alpha titanium alloy, Scripta Metallurgica 21 (4) (1987) 469–474. doi:10.1016/0036-9748(87)90183-9.

[3] BEA, Accident to the AIRBUS A380-861 registered F-HPJE and operated by Air France on 30/09/2017 en route over Greenland [Investigation delegated to BEA by the authorities of Denmark], 2020.
URL `https://bea.aero/en/investigation-reports/notified-events/detail/accident-to`

[4] Pratt, Whitney, Metallurgical Investigation of Fan Blades No. 11 and No. 10 from PW4077 Engine 777049., 2018.
URL `https://data.ntsb.gov/Docket/?NTSBNumber=DCA18IA092`

[5] M. Bache, A review of dwell sensitive fatigue in titanium alloys: the role of microstructure, texture and operating conditions, International Journal of Fatigue 25 (9–11) (2003) 1079–1087. doi:10.1016/S0142-1123(03)00145-2.

[6] P. C. Ruffles, The History of the Rolls-Royce RB211 Turbofan Engine, Rolls-Royce Heritage Trust, 2014.

[7] D. S. McDarmaid, A. W. Bowen, P. G. Partridge, Superplastic deformation of strongly textured Ti-6Al-4V, Journal of Materials Science 20 (6) (1985) 1976–1984. doi:10.1007/BF01112279.

[8] U. Kansal, M. E. Kassner, D. R. Hiatt, B. M. Bristow, Microstructural banding in thermally and mechanically processed titanium 6242, Journal of Materials Engineering and Performance 1 (3) (1992) 393–398. doi:10.1007/BF02652394.

[9] A. Woodfield, M. Gorman, R. Corderman, J. Sutliff, B. Yamrom, Effect of microstructure on dwell fatigue behavior of Ti-6242, in: Titanium' 95: Science and Technology, Vol. 2, Birmingham, UK, 1995, p. 1116–1123.

[10] G. Bailey, R. Dimlich, K. Alexander, J. McCarthy, T. Pretlow, A. P. Woodfield, J. A. Sutliff, The influence of microtexture on fatigue behavior in titanium alloys, Microscopy and Microanalysis 3 (S2) (1997) 571–572. doi:10.1017/S1431927600009740.

[11] D. J. Dingley, V. Randle, Microtexture determination by electron backscatter diffraction, Journal of Materials Science 27 (17) (1992) 4545–4566. doi:10.1007/BF01165988.

[12] V. Randle, Microtexture Determination and Its Applications, Institute of Materials, 1992.

[13] R. J. Wilson, V. Randle, W. J. Evans, The influence of the burgers relation on crack propagation in a near α-titanium alloy, Philosophical Magazine A 76 (2) (1997) 471–480. doi:10.1080/01418619708209986.

[14] K. Le Biavant, S. Pommier, C. Prioul, Local texture and fatigue crack initiation in a Ti-6Al-4V titanium alloy, Fatigue & Fracture of Engineering Materials & Structures 25 (6) (2002) 527–545. doi:10.1046/j.1460-2695.2002.00480.x.

[15] V. Sinha, M. J. Mills, J. C. Williams, J. E. Spowart, Observations on the faceted initiation site in the dwell-fatigue tested ti-6242 alloy: Crystallographic orientation and size effects, Metallurgical and Materials Transactions A 37 (5) (2006) 1507–1518. doi:10.1007/s11661-006-0095-x.

[16] A. L. Pilchak, C. J. Szczepanski, J. A. Shaffer, A. A. Salem, S. L. Semiatin, Characterization of microstructure, texture, and microtexture in near-alpha titanium mill products, Metallurgical and Materials Transactions A 44 (11) (2013) 4881–4890. doi:10.1007/s11661-013-1804-x.

[17] P. Ari-Gur, S. L. Semiatin, Evolution of microstructure, macrotexture and microtexture during hot rolling of Ti-6A1-4V, Materials Science and Engineering: A 257 (1) (1998) 118–127. doi:10.1016/S0921-5093(98)00829-6.

[18] L. Germain, N. Gey, M. Humbert, P. Vo, M. Jahazi, P. Bocher, Texture heterogeneities induced by subtransus processing of near α titanium alloys, Acta Materialia 56 (16) (2008) 4298–4308. doi:10.1016/j.actamat.2008.04.065.

[19] L. Germain, N. Gey, M. Humbert, P. Bocher, M. Jahazi, $\beta \rightarrow \alpha$s variant selection in sharp hcp textured regions of a bimodal IMI834 billet, in: Materials Science Forum, Vol. 495–497, Trans Tech, Leuven, Belgium, 2005, p. 663–668. doi:10.4028/www.scientific.net/MSF.495-497.663.
URL `http://www.scientific.net/MSF.495-497.663`

[20] R. Ma, A. L. Pilchak, S. L. Semiatin, T. J. Truster, Modeling the evolution of microtextured regions during α/β processing using the crystal plasticity finite element method, International Journal of Plasticity 107 (2018) 189–206. doi:10.1016/j.ijplas.2018.04.004.

[21] Z. X. Zhang, S. J. Qu, A. H. Feng, X. Hu, J. Shen, Microstructural mechanisms during multidirectional isothermal forging of as-cast Ti-6Al-4V alloy with an initial lamellar microstructure, Journal of Alloys and Compounds 773 (2019) 277–287. doi:10.1016/j.jallcom.2018.09.220.

[22] J. L. W. Warwick, N. G. Jones, I. Bantounas, M. Preuss, D. Dye, In situ observation of texture and microstructure evolution during rolling and globularization of Ti–6Al–4V, Acta Materialia 61 (5) (2013) 1603–1615. doi:10.1016/j.actamat.2012.11.037.

[23] FAA, Ac 33.70-3 - damage tolerance for material anomalies in titanium life-limited turbine engine rotors (Apr 2023).

[24] W. J. Evans, M. R. Bache, Dwell-sensitive fatigue under biaxial loads in the near-alpha titanium alloy IMI685, International Journal of Fatigue 16 (7) (1994) 443–452. doi:10.1016/0142-1123(94)90194-5.

[25] F. P. E. Dunne, D. Rugg, A. Walker, Lengthscale-dependent, elastically anisotropic, physically-based hcp crystal plasticity: Application to cold-dwell fatigue in Ti alloys, International Journal of Plasticity 23 (6) (2007) 1061–1083. doi:10.1016/j.ijplas.2006.10.013.

[26] K. Kapoor, R. Noraas, V. Seetharaman, M. D. Sangid, Modeling strain localization in microtextured regions in a titanium alloy: Ti-6Al-4V, Integrating Materials and Manufacturing Innovation 8 (4) (2019) 455–467. doi:10.1007/s40192-019-00159-y.

[27] A. Moreau, L. Toubal, P. Bocher, M. Humbert, E. Uta, N. Gey, Evaluation of macrozone dimensions by ultrasound and EBSD techniques, Materials Characterization 75 (2013) 115–128. doi:10.1016/j.matchar.2012.09.011.

[28] B. Fernández Silva, M. Jackson, K. Fox, B. P. Wynne, Tool for automatic macrozone characterization from EBSD data sets of titanium alloys, Journal of Applied Crystallography 56 (33) (2023) 737–749. doi:10.1107/S1600576723003862.

[29] J. Shen, V. Venkatesh, R. Noraas, S. Ghosh, Parametrically upscaled crack nucleation model (PUCNM) for fatigue nucleation in titanium alloys containing micro-texture regions (MTR), Acta Materialia 252 (2023) 118929. doi:10.1016/j.actamat.2023.118929.

[30] Y. Liu, F. P. E. Dunne, The mechanistic link between macrozones and dwell fatigue in titanium alloys, International Journal of Fatigue 142 (2021) 105971. doi:10.1016/j.ijfatigue.2020.105971.

[31] J. R. James, R. John, S. Jha, A. L. Pilchak, R. Arroyave, E. J. Payton, Effect of microtextured region stereology on crack growth lifetime predictions in Ti-6Al-4V, JOM 74 (10) (2022) 3720–3732. doi:10.1007/s11837-022-05462-2.

[32] I. Bantounas, D. Dye, T. C. Lindley, The effect of grain orientation on fracture morphology during high-cycle fatigue of Ti-6A1-4V, Acta Materialia 57 (12) (2009) 3584–3595. doi:10.1016/j.actamat.2009.04.018.

[33] T. B. Britton, S. Birosca, M. Preuss, A. J. Wilkinson, Electron backscatter diffraction study of dislocation content of a macrozone in hot-rolled Ti-6A1-4V alloy, Scripta Materialia 62 (9) (2010) 639–642. doi:10.1016/j.scriptamat.2010.01.010.

[34] M. Anahid, M. K. Samal, S. Ghosh, Dwell fatigue crack nucleation model based on crystal plasticity finite element simulations of polycrystalline titanium alloys, Journal of the Mechanics and Physics of Solids 59 (10) (2011) 2157–2176. doi:10.1016/j.jmps.2011.05.003.

[35] Z. Zheng, D. S. Balint, F. P. E. Dunne, Dwell fatigue in two Ti alloys: An integrated crystal plasticity and discrete dislocation study, Journal of the Mechanics and Physics of Solids 96 (2016) 411–427. doi:10.1016/j.jmps.2016.08.008.

[36] M. A. Cuddihy, A. Stapleton, S. Williams, F. P. E. Dunne, On cold dwell facet fatigue in titanium alloy aero-engine components, International Journal of Fatigue 97 (2017) 177–189. doi:10.1016/j.ijfatigue.2016.11.034.

[37] A. Naït-Ali, S. Hémery, M. Gueguen, How macrozone size and morphology influence yield in titanium alloys investigated using fast fourier transform-based crystal plasticity simulations, International Journal of Solids and Structures 216 (2021) 1–16. doi:10.1016/j.ijsolstr.2021.01.008.

[38] J. Wendorf, P. R. Dawson, T. M. Pollock, Grain-scale stress states in microtextured Ti64: Implications for dwell fatigue, JOM 74 (10) (2022) 3709–3719. doi:10.1007/s11837-022-05423-9.

[39] M. E. Kandaoui, F. Scandella, L. Germain, P. Brandy, D. Debreyer, C. Gérardin, Éric Fleury, Microstructure and Mechanical Properties of Ti-6Al-4V Laser Welds for Airplane Floor Manufacturing Application, John Wiley & Sons, Ltd, 2016, Ch. 260, pp. 1551–1556. doi:10.1002/9781119296126.ch260.

[40] H. Inagaki, Evolution of textures and microstructures in thermomechanical processing of ti-6al-4v, International Journal of Materials Research 81 (6) (1990) 433–445. doi:10.1515/ijmr-1990-810608.

[41] B. Beausir, J.-J. Fundenberger, Analysis tools for electron and x-ray diffraction, atex - software, Université de Lorraine - Metz (2017).
URL `www.atex-software.eu`

[42] R. A. Lebensohn, A. K. Kanjarla, P. Eisenlohr, An elasto-viscoplastic formulation based on fast fourier transforms for the prediction of micromechanical fields in polycrystalline materials, International Journal of Plasticity 32-33 (2012) 59–69. doi:10.1016/j.ijplas.2011.12.005.

[43] H. Moulinec, P. Suquet, A fast numerical method for computing the linear and non linear properties of composites, C. R. Acad. Sci. Paris II 318 (1994) 1417–1423.

[44] H. Moulinec, P. Suquet, A numerical method for computing the overall response of nonlinear composites with complex microstructure, Computer Methods in Applied Mechanics and Engineering 157 (1) (1998) 69–94. doi:10.1016/S0045-7825(97)00218-1.

[45] B. Anglin, R. A. Lebensohn, A. D. Rollett, Validation of a numerical method based on Fast Fourier Transforms for heterogeneous thermoeastic materials by comparison with analytical solutions, Computational Materials Science 87 (2014) 209–217. doi:10.1016/j.commatsci.2014.02.027.

[46] F. Willot, Fourier-based schemes for computing the mechanical response of composite with accurate local field, C. R. Mecanique 343 (2015) 232–245. doi:10.1016/j.crme.2014.12.005.

[47] K. Eloh, A. Jacques, S. Berbenni, Development of a new consistent discrete Green operator for FFT-based methods to solve heterogeneous problems with eigenstrains, International Journal of Plasticity 116 (2019) 1–23. doi:10.1016/j.ijplas.2018.10.011.

[48] J. C. Michel, H. Moulinec, P. Suquet, A computational scheme for linear and non-linear composites with arbitrary phase contrast, International Journal for Numerical Methods in Engineering 52 (1-2) (2001) 139–160. doi:10.1002/nme.275.

[49] M. Zecevic, R. A. Lebensohn, L. Capolungo, New large-strain fft-based formulation and its application to model strain localization in nano-metallic laminates and other strongly anisotropic crystalline materials, Mechanics of Materials 166 (2022) 104208. doi:10.1016/j.mechmat.2021.104208.

[50] M. Frigo, S. G. Johnson, The design and implementation of FFTW3, Proc. IEEE 93 (2) (2005) 216–231. doi:10.1109/JPROC.2004.840301.

[51] V. Tari, R. A. Lebensohn, R. Pokharel, T. J. Turner, P. A. Shade, J. V. Bernier, A. D. Rollett, Validation of micro-mechanical FFT-based simulations using High Energy Diffraction Microscopy on Ti-7Al, Acta Materialia 154 (2018) 273–283. doi:10.1016/j.actamat.2018.05.036.

[52] J. J. Bhattacharyya, S. Nair, D. C. Pagan, V. Tari, R. A. Lebensohn, A. D. Rollett, S. R. Agnew, Elastoplastic transition in a metastable β-Titanium alloy, Timetal-18 – an in-situ synchrotron X-ray diffraction study, International Journal of Plasticity 139 (2021) 102947. doi:10.1016/j.ijplas.2021.102947.

[53] A. Kulkarni, J. Kovačević, F. Franchetti, Massive scaling of MASSIF: Algorithm Development and Analysis for Simulation on GPUs, in: Proceedings of the Platform for Advanced Scientific Computing Conference, PASC '20, Association for Computing Machinery, New York, NY, USA, 2020, p. 1–10. doi:10.1145/3394277.3401857.
URL `https://dl.acm.org/doi/10.1145/3394277.3401857`

[54] G. Lütjering, J. C. Williams, Titanium (2nd ed.), Springer, 2007.

[55] R. Asaro, A. Needleman, Overview no. 42 texture development and strain hardening in rate dependent polycrystals, Acta Metallurgica 33 (1985) 923–953. doi:10.1016/0001-6160(85)90188-9.

[56] S. Hémery, A. Naït-Ali, M. Guéguen, J. Wendorf, A. T. Polonsky, M. P. Echlin, J. C. Stinville, T. M. Pollock, P. Villechaise, A 3d analysis of the onset of slip activity in relation to the degree of micro-texture in ti–6al–4v, Acta Materialia 181 (2019) 36–48.

[57] K. P. Mingard, P. N. Quested, M. S. Peck, Determination of grain size by EBSD - Report on a round robin measurement of equiaxed titanium., 2012.
URL https://eprintspublications.npl.co.uk/5412/

[58] J. Ahrens, B. Geveci, C. Law, ParaView: An end-user tool for large data visualization, in: Visualization Handbook, Elesvier, 2005, ISBN 978-0123875822.

[59] A. M. Stapleton, S. L. Raghunathan, I. Bantounas, H. J. Stone, T. C. Lindley, D. Dye, Evolution of lattice strain in ti–6al–4v during tensile loading at room temperature, Acta Materialia 56 (2008) 6186–6196. doi:doi:10.1016/j.actamat.2008.08.030.

[60] M. P. Echlin, J. C. Stinville, V. M. Miller, W. C. Lenthe, T. R. Pollock, Incipient slip and long range plastic strain localization in microtextured ti-6al-4v titanium, Acta Materialia 114 (2016) 164–175. doi:doi.org/10.1016/j.actamat.2016.04.057.

[61] S. Sharifimehr, A. Fatemi, On the interaction of normal and shear stresses in multiaxial fatigue damage, Fatigue & Fracture of Engineering Materials & Structures 42 (2019) 2000–2016. doi:10.1111/ffe.13070.

[62] K. Prasad, R. Sarkar, V. Singh, P. Ghosal, A. Bhattacharjee, H. Gokhale, On the probabilistic assessment of variability in fatigue life in a near α titanium alloy Timetal 834: Crystallography of fatigue crack initiating facets, Acta Materialia 218 (2021) 117214. doi:https://doi.org/10.1016/j.actamat.2021.117214.

[63] A. L. Pilchak, A simple model to account for the role of microtexture on fatigue and dwell fatigue lifetimes of titanium alloys, Scripta Materialia 74 (2014) 68–71. doi:10.1016/j.scriptamat.2013.10.024.

[64] S. Berbenni, V. Taupin, R. A. Lebensohn, A fast Fourier transform-based mesoscale field dislocation mechanics study of grain size effects and reversible plasticity in polycrystals, Journal of the Mechanics and Physics of Solids 135 (2020) 103808. doi:10.1016/j.jmps.2019.103808.

Appendix A. Schematic figures of considered macrozone morphologies with different volume fractions

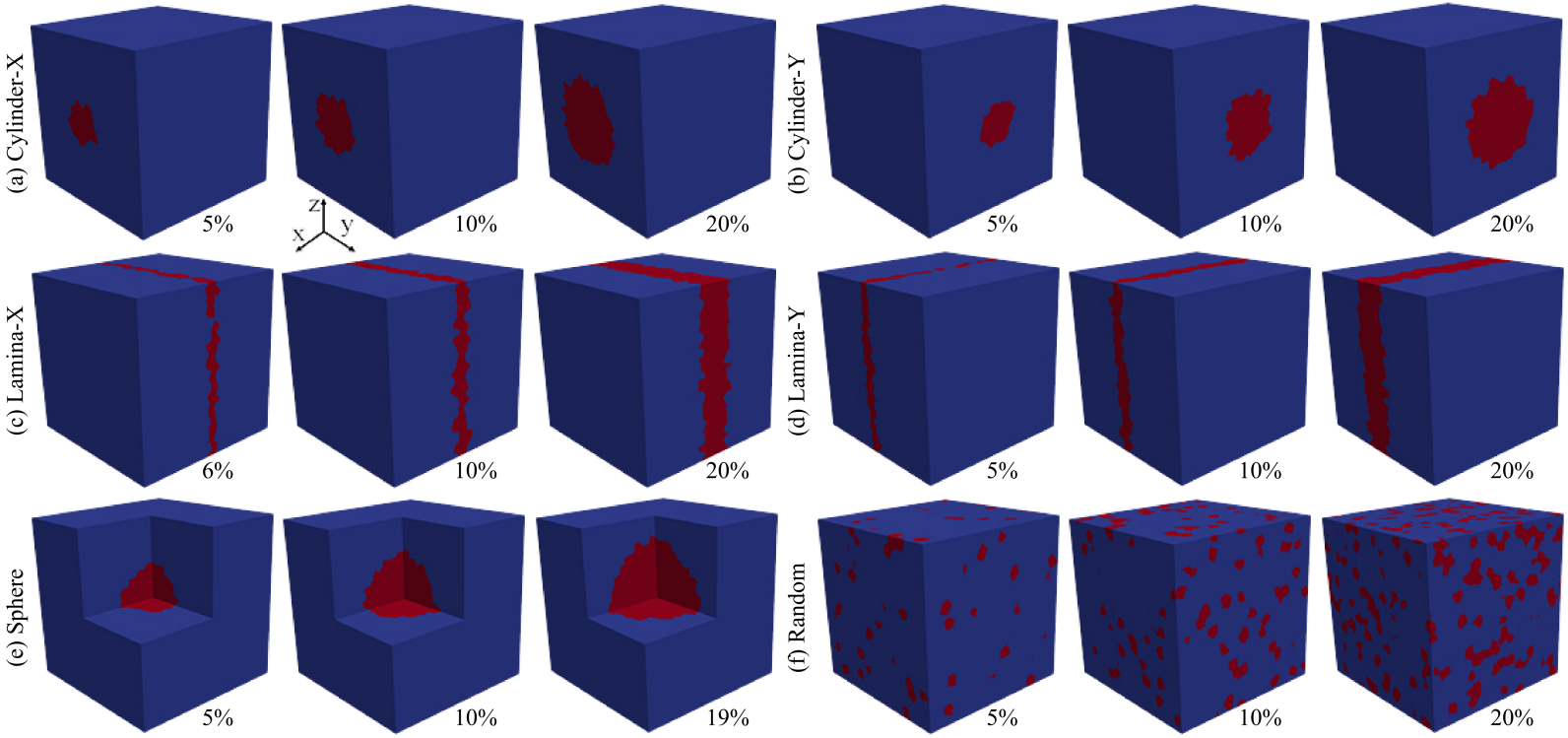

Figure A.15: Schematic figures of the considered morphologies of the macrozone with different volume fractions. The red color indicates the macrozone while the blue is for general grains.